Nanoscale Advances

ROYAL SOCIETY OF CHEMISTRY

PAPER

View Article Online
View Journal | View Issue

Cite this: *Nanoscale Adv.*, 2025, **7**, 5067

Boosting turquoise hydrogen and carbon nanotube production *via* catalytic methane decomposition: influence of active metal ratios in Fe5–Co–Zn/γ-Al_2O_3 nanocatalysts†

Aakash Rajpoot, [a] Afaq Ahmad Khan [a] and Ejaz Ahmad *[ab]

Received 12th March 2025
Accepted 3rd July 2025

DOI: 10.1039/d5na00237k

rsc.li/nanoscale-advances

The present study reports the synthesis of a series of nanocatalysts (NCs) comprising iron (Fe), cobalt (Co), and zinc (Zn) supported on γ-Al_2O_3 nanopowder (Fe5–Co–Zn/γ-Al_2O_3) by tuning the metals stoichiometric ratio using a facile co-precipitation approach. The powder X-ray diffraction patterns and Raman spectra revealed that the freshly synthesized Fe5–Co–Zn/γ-Al_2O_3 is composed of hexagonal Fe_2O_3, cubic Co_3O_4, and hexagonal ZnO phases. The NCs exhibited efficient performance in CH_4 decomposition, yielding turquoise hydrogen (H_2) and carbon nanotubes (CNTs) as solid carbon by-products. The active metals consisted of 50% Fe, 5% Co, and 15% Zn as Fe5Co0.5Zn1.5 given a maximum CH_4 conversion of 90% and an H_2 yield of 92.2%, which are considerably higher than those of many other previously reported NCs. The structural characteristics of the spent NCs (S-Fe5Co2Zn0 to S-Fe5Co0Zn2) were examined, showing variation in the growth and quality of CNT. Moreover, the electron microscopy micrographs suggested that the CNTs growth plausibly followed the base-growth model. The CNTs are also effectively isolated from spent NCs. This study paves the way for a streamlined approach to designing and unravelling the intricate distribution of active metals on suitable supports, offering deeper insights into optimizing CH_4 decomposition into H_2 and high-quality CNTs.

1 Introduction

The growing population and economic development have led to a heightened demand for energy from fossil fuels, resulting in increased greenhouse gas emissions, such as carbon dioxide. Consequently, finding alternative clean energy sources has become a significant challenge.[1] The development of renewable energy technology aims to achieve a low-carbon energy system and economy. However, the shift towards a low-carbon economy will necessitate the creation of groundbreaking solutions and the ongoing use of fossil fuels for many years. Nevertheless, hydrogen (H_2) is widely regarded as an immensely pristine and environmentally friendly energy source. Its demand has surged by over 50% in the last few decades and continues to grow rapidly worldwide.[2] There is an urgent requirement for the advancement of H_2 production methods that are both clean and free from CO_2 emissions.[3–5] The rise in the requirement of zero-emission fuel in the automotive sector, space technology, and power systems is attributable to the fact that H_2 can be a vital energy source.[6,7] Currently, H_2 can be produced using various processes such as the electrolysis of water,[8] coal and biomass gasification[9,10] and pyrolysis of natural gas.[11] There is a trade-off between the significant energy expenditure required to produce hydrogen by electrolysis and coal/biomass gasification.[12]

In contrast, natural gas is a widely used fossil fuel made primarily of 70% to 95% methane (CH_4) and possesses high transportability. CH_4 can be converted into H_2 using several processes, such as partial oxidation,[13] steam reforming,[14] plasma reforming,[15] and catalytic decomposition.[16] Catalytic methane decomposition (CMD) is a highly promising process that can generate hydrogen without emitting CO or CO_2 and requires less energy than steam and plasma reforming procedures.[12] The CDM process is an endothermic reaction, as shown by the following equation:

$$CH_4 = C + 2H_2 \quad \Delta H^{\circ}_{298K} = 74.85 \text{ kJ mol}^{-1} \qquad (1)$$

The process is widely recognized as pyrolysis of methane, sometimes known as thermal methane cracking.[17] The CDM process can also be carried out at an operating temperature of around ~700 to ~900 °C. The choice of a catalyst plays a crucial role in reducing the necessary temperature and increasing the

[a]GreenCat Laboratory, Department of Chemical Engineering, Indian Institute of Technology (Indian School of Mines), Dhanbad, 826004, India. E-mail: ejaz@iitism.ac.in

[b]Naresh Vashisht Centre for Hydrogen and CCUS Technologies, Indian Institute of Technology (Indian School of Mines), Dhanbad, 826004, India

† Electronic supplementary information (ESI) available. See DOI: https://doi.org/10.1039/d5na00237k

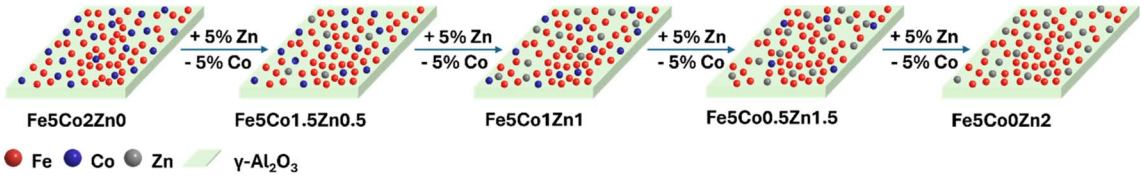

Scheme 1 A schematic illustration of the cobalt (Co) and zinc (Zn) stoichiometric ratio-controlled synthesis of trimetallic Fe5–Co–Zn/γ-Al_2O_3 nanocatalysts.

amount of desired product formation. Several factors influence CDM efficiency, including the catalyst metal type/composition, the support material type, and the interactions between the catalyst and support.[18] The catalyst support must have thermal, chemical, and mechanical stability to ensure process safety and consistency. Additionally, it should offer a large surface area to facilitate the uniform distribution of active sites.[19] Furthermore, the experimental reaction conditions influence the catalyst/support performance in CDM processes.[20] The catalysts originated from group VIII, including nickel (Ni), cobalt (Co), and iron (Fe), are highly regarded for their exceptional catalytic capabilities and cost-effectiveness in the CDM process.[21] The Ni-based catalysts have shown high activity in CH_4 decomposition. However, it is highly prone to coking (carbon deposition), short lifespan, sintering, high-temperature stability, selectivity concerns, *etc.*[16,22,23] As a consequence, the incorporation of Co and Fe into Ni-based catalysts has been studied to improve their performance and durability.[24–26] However, the process of restoring deactivated Ni-based catalysts is still uncertain and not commercially viable at present. The researchers also developed beyond Ni-based catalysts such as 60%Fe/Al_2O_3,[27] 60%Fe/CeO_2,[28] Co/SiO_2, Co/Nb_2O_5,[18] Co/γ-Al_2O_3,[29] and Zn–$CoFe_2O_4$,[30] $ZnFe_2O_4$.[31] Nevertheless, efforts are underway to develop an ideal catalyst to achieve a high turquoise hydrogen yield and produce high-quality solid carbon material.

Numerous investigations focused on CMD reactions indicate that the advancement of tri-metallic catalysts shows greater potential for enhancing reactivity and durability at ideal CH_4 conversion temperatures.[32] The non-noble metals-based trimetallic catalysts are promising and cost-effective due to their range of adjustable physicochemical properties. Fe-based catalyst is an attractive contender in CMD because of its low cost and partially full 3d orbitals, which allow it to assist the dissociation of hydrocarbons. Catalysts with added cobalt operate at lower temperatures and exhibit greater catalytic activity compared to those with only Fe-catalyst.[33,34] The catalytic stability is also affected by the type of support utilized in catalyst preparation. Various supports are reported, such as Al_2O_3, La_2O_3, SiO_2, MgO, H-ZSM-5, CeO_2, TiO_2, and CaO, to synthesize catalysts for CMD.[35,36] Among these supports, Al_2O_3 has emerged as a promising choice for the CMD, probably due to its extensive specific surface area, effective interaction between metal and support, and excellent stability.[37] In comparison, SiO_2 demonstrates weak metal–support bonding, low acidity, and inadequate thermal stability, making it susceptible to metal sintering and carbon deposition.[35] CeO_2, on the other hand, contains abundant surface oxygen species that facilitate the oxidation of carbon deposits and the reoxidation of metal sites. Nevertheless, it suffers from moderate acidity, a relatively small surface area, poor thermal stability, and reduced reducibility due to solid solution formation.[35,38] Meanwhile, TiO_2 facilitates CH_4 activation and dissociation, the formation of reduced TiO_x species during the reaction can lead to the coverage of active metal particles. This encapsulation phenomenon potentially blocks active site accessibility, consequently impairing catalytic performance.[35] So, the selection of Al_2O_3 as a support is a suitable choice to synthesize a catalyst for efficient methane decomposition.[35,38] While there have been notable progressions in the synthesis of tri-metallic catalysts, the ability to Fe, Co, and Zn-based catalysts with controlled stoichiometry remains unachieved.

Herein, we report the synthesis of trimetallic Fe5–Co–Zn/γ-Al_2O_3 nanocatalysts (NCs) with tunable Co and Zn stoichiometry for CH_4 decomposition in a temperature-programmed surface reaction (Scheme 1). The addition of Zn to Fe–Co catalysts is intended to study its role in improving dispersion, modifying metal-support interactions, and enhancing solid carbon structure, which can enhance catalytic efficiency and durability. The potential synergistic effects between these metals remain understudied, highlighting the novelty of this research work. The nanocatalysts were designed with a constant alumina support (30 wt%) and fixed Fe (50 wt%) content while varying the Co and Zn content from 0 to 20 wt% through a co-precipitation method. The synthesized nanocatalysts (NCs) exhibited effective performance in breaking down CH_4, resulting in the production of turquoise hydrogen (H_2) and carbon nanotubes (CNTs) as solid carbon by-products. Further, the reactivity for CH_4 conversion, H_2 yields, and the effect of reaction time of the various synthesized nanocatalysts are studied. Additionally, various analytical techniques were utilized to investigate the physico-chemical characteristics of fresh, reduced, and spent nanocatalysts.

2 Experimental section

2.1 Materials

Iron(III) nitrate nonahydrate [$Fe(NO_3)_2 \cdot 9H_2O$, 98%], cobalt(II) nitrate hexahydrate [$Co(NO_3)_2 \cdot 6H_2O$, 99%], zinc(II) nitrate hexahydrate [$Zn(NO_3)_2 \cdot 6H_2O$, 99%], gamma alumina (γ-Al_2O_3) nanopowder, 99.5%, sodium dodecyl sulfate ($CH_3(CH_2)_{11}$-SO_4Na), sodium hydroxide and (NaOH), were purchased from Sigma-Aldrich and SRL chemicals, and utilized without any further purification. Throughout the experiments, double-distilled water was consistently utilized.

2.2 Synthesis of Fe5–Co–Zn/γ-Al_2O_3 NCs

Herein, Fe5–Co–Zn/γ-Al_2O_3 NCs with stoichiometrically tunned metal compositions were synthesized *via* the co-precipitation method (Table S1†). Metal nitrates such as $Fe(NO_3)_2 \cdot 9H_2O$, $Co(NO_3)_2 \cdot 6H_2O$, and $Zn(NO_3)_2 \cdot 6H_2O$ were used as a metal precursor. Fe5Co2Zn0, Fe5Co1.5Zn0.5, Fe5Co1Zn1, Fe5Co0.5Zn1.5, and Fe5Co2Zn0 supported on γ-Al_2O_3 nanopowder are synthesized by controlling the ratio of Co and Zn from 0 to 20 weight percent (wt%). The prerequisite amounts of iron (Fe), cobalt (Co), and zinc (Zn) salts were dissolved in 50 mL of double distilled water, and 30 wt% of γ-Al_2O_3 nanopowder was added into the metal salt solution. After that, 2 M NaOH aqueous solution was gradually added to reach a solution pH of ~9, and then the mixture was stirred continuously for five hours. The precipitates were then collected, washed with distilled water, and separated by centrifugation. Afterward, the precipitate was dried at 120 °C overnight and calcined at 750 °C for 5 hours at 3 °C min^{-1} of heating rate to obtain the final NCs. Before each CH_4 decomposition reaction, the NCs underwent *in situ* reduction by exposing the NCs to a 1 : 9 of H_2 and argon (Ar) gas mixture at a total flow rate of 30 mL min^{-1} at 750 °C and 1 atm pressure.

2.3 Characterization

A Pan Analytics X-ray diffractometer was employed to analyse the crystal structures of all NCs. Powder-XRD patterns were displayed within the 10° to 90° 2θ range using a current of 10 milliamperes and an applied voltage of 30 kV. The scanning pace was set at 4° per minute, and a Cu–K radiation source was employed. The valence state and chemical composition are ascertained by means of X-ray photoelectron spectroscopy (XPS) with an Al Kα radiation source of 1486.6 eV (PHI 5000 Versaprobe III). Determining the metal concentration that was present in the NCs using an ICP-OES system (iCAP 7400 Duo, Thermo Fisher Scientific, USA). Temperature-programmed reduction (TPR) study was performed on the calcined NCs using Quantachrome instruments (Boynton Beach, FL 33426). N_2 adsorption–desorption studies carried out with a Micromeritics Instrument Corporation, USA, 3FLEX 3500 analyzer. The HORIBA Scientific, France LabRAM HR-UV-Open InVia Raman microscope was used to obtain Raman spectra of the freshly and spent NCs. The excitation wavelength was 532 nm and the laser intensity was 5 mW. The morphology of fresh and spent NCs were analyzed using a field emission scanning electron microscope (FE-SEM), *via* Supra 55 made by Zeiss, Germany. The transmission electron microscopy (TEM), high-resolution TEM with scanning transmission electron microscopy-energy dispersive X-ray spectroscopy (STEM-EDS) techniques were employed to obtain micrographs of the NCs using a high-resolution Thermo Scientific Talos F200X G2 operating at 200 kV. In addition, the elemental composition of the spent NCs was evaluated using a CHNS analysis using an Elementar vario MICRO equipment. Fourier Transform Infrared Spectroscopy (FTIR) is employed to analyse the functional groups present within a spent NCs using the BRUKER ALPHA-II instrument.

2.4 Catalytic methane decomposition process

The methane decomposition experiments were carried out at a reaction temperature of 750 °C under standard atmospheric pressure. The reactions were performed in a quartz tube that had an interior diameter of 0.013 m and a height of 0.16 m. A 50 mg nanocatalyst was accurately positioned at the bottom of the reactor using quartz wool. Before initiating the reaction, the *in situ* reduction was conducted at the same temperature for a duration of 120 minutes in the presence of hydrogen. We have used diluted hydrogen (10% H_2) to achieve a more gradual and controlled reduction, which helps to prevent the sintering of metal particles and preserves their dispersion.[39] Moreover, pure hydrogen is highly flammable and can be hazardous at high temperatures, especially in a laboratory. Furthermore, using a diluted mixture enhances safety while also protecting the structural integrity of the catalyst by avoiding rapid reduction that could lead to phase changes or material degradation.[40]

Subsequently, the quartz tube underwent degassing with argon for 60 minutes to establish an inert environment. Following this, the methane and argon gases were introduced into the system at a volume ratio of 1 : 19 and maintained at this ratio throughout the 150 minute reaction period. Additionally, the space velocity was held constant at 1.2 litre per hour per gram of NCs. The outlet of the reactor was connected to a mass spectroscopy apparatus equipped with a thermal conductivity detector (TCD) for the examination and determination of composition and molecular weight. The conversion of methane, the yield of turquoise hydrogen, and carbon production were determined utilizing eqn (2) and (3).

$$CH_4 \text{ conversion } (\%) = \frac{\text{methane}_{in} - \text{methane}_{out}}{\text{methane}_{in}} \times 100 \quad (2)$$

$$H_2 \text{ yield } (\%) = \frac{\text{hydrogen moles produced}}{\text{methane moles in feed} \times 2} \times 100 \quad (3)$$

3 Results and discussion

3.1 Structural characterization

Fig. 1a shows the powder X-ray diffraction patterns of the synthesized NCs, Fe5Co2Zn0 to Fe5Co0Zn2 supported on γ-Al_2O_3. The diffraction pattern of Fe5Co2Zn0 showed that the intense peaks of 2θ at 24.1° (012), 33.2° (104), and 35.6° (110) have resembled with standard diffraction peaks of the hexagonal phase of Fe_2O_3 (JCPDF no. 01-5840, $a = b = 5.038$ Å; $c = 13.772$ Å). The characteristic peak observed at 18.3° (111) and 30.3° (022) confirmed the formation of the cubic phase of Co_3O_4 (JCPDF no. 06-9372, $a = b = c = 8.189$ Å) along with hexagonal Fe_2O_3. A small intensity at 66.8° of the planes (440) indicates the presence of γ-Al_2O_3. With an increase in Zn wt% and a decrease in Co wt%, the new diffraction peaks of (004) and (022) plane were observed for Fe5Co1.5Zn0.5 to Fe5Co0.5Zn1.5 with a spontaneous decrease of (111) peak intensity, suggesting the formation of hexagonal phase of ZnO (JCPDF no. 06-5122, $a = b = 3.265$ Å; 5.219 Å) along with hexagonal Fe_2O_3 and cubic Co_3O_4. Further increase in Zn wt%, the (111) peak has

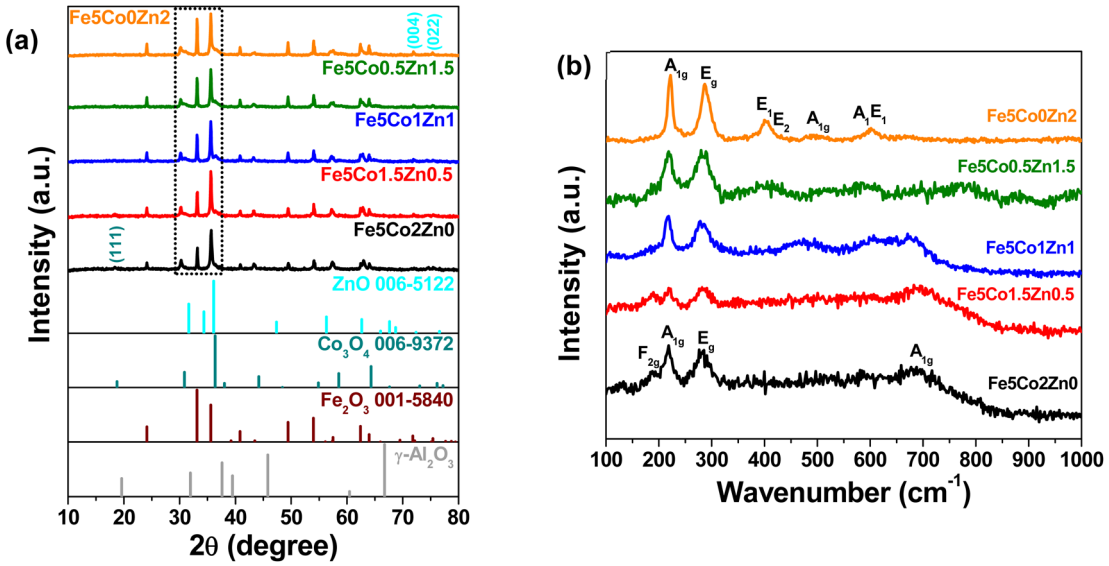

Fig. 1 (a) Powder-XRD diffraction patterns of the freshly synthesized Fe5–Co–Zn/γ-Al_2O_3 nanocatalyst at different ratios of Co and Zn with corresponding standard diffraction profiles, and (b) Raman spectra of the freshly synthesized Fe5–Co–Zn/γ-Al_2O_3 nanocatalysts in the spectral range 100 cm^{-1} –1000 cm^{-1} (λ = 532 nm).

completely disappeared, and the intensity of (004) and (022) peaks are increased that attributed only hexagonal ZnO along hexagonal Fe_2O_3 existed in the Fe5Co0Zn2. The diffraction patterns show that Fe5Co2Zn0 contains a mixture of Co_3O_4 and Fe_2O_3 phases, while Fe5Co0Zn2 exhibits ZnO and Fe_2O_3. However, Fe5Co1.5Zn0.5 to Fe5Co0.5Zn1.5 contains Co_3O_4, ZnO and Fe_2O_3. The peak intensity ratio of 33.2° and 35.6° indicated that the ZnO content rises as the Zn wt% increases from 5% to 20% in the nanocatalyst. The crystallite size of catalysts plays a significant role in the catalytic methane decomposition reaction. The interplanar spacing and crystallite sizes of the catalysts, derived from their diffraction profiles, are presented in Table S2.† Using the Debye–Scherrer equation ($D = k\lambda/\beta \cos\theta$), the average crystallite size of the fresh catalysts was found to range between 30.8 and 38.2 nm. Notably, Fe5Co0.5Zn1.5 showed the smallest crystallite size at 30.8 nm, indicating its potential significance in improving methane decomposition.

Raman spectroscopic analysis was also performed to confirm the formation of Co_3O_4, ZnO, and Fe_2O_3 in Fe5Co2Zn0 to Fe5Co0Zn2 (Fig. 1b). The two peaks with the frequency of 194.1 and 689.8 cm^{-1} in Fe5Co2Zn0 denoted as Raman active modes F 2g and A 1g, respectively is well aligned with the Co_3O_4.[41] Furthermore, an increased in Zn wt% with decreasing Co wt% (Fe5Co1.5Zn0.5 to Fe5Co0.5Zn1.5), new peaks appeared along with the Co_3O_4 Raman peaks. Further, the increase in Zn wt% (Fe5Co0Zn2), F 2g (194.1 cm^{-1}), and A 1g (689.8 cm^{-1}) modes have completely disappeared. However, four peaks with the frequency of 403, 433, 591, and 615 cm^{-1} assigned as Raman active modes of E1, E2, A1, and E1, respectively, corresponded to the ZnO.[42] Additionally, the two most prominent peaks detected in all NCs correspond to the primary Raman active bands, identified as A 1g and E_g, which are attributed to the α-Fe_2O_3 phase.[43] So, the Raman results also correspond to our powder-XRD outcomes and indicate that the synthesized trimetallic nanocatalysts are composed of Co_3O_4, ZnO, and α-Fe_2O_3.

X-ray photoelectron spectroscopy (XPS) analysis of freshly synthesized trimetallic Fe5Co1.5Zn0.5, Fe5Co1Zn1, and Fe5Co0.5Zn1.5 was performed to investigate the chemical composition and electronic state on the surface of the NCs. The survey spectrum peaks clearly indicate that the NCs are composed of iron (Fe), cobalt (Co), zinc (Zn), aluminium (Al), and oxygen (O) elements (Fig. S1a†). The core-level spectra of Fe 2p, Co 2p, Zn 2p, O 1s, and Al 2p were deconvoluted to investigate the valence state present in the trimetallic NCs (Fig. 2 and S1†). The obtained binding energies of the valence states are presented in Table S3.† The core-level spectrum of Fe 2p is fitted into two pairs of peaks ($2p_{3/2}$ and $2p_{1/2}$), with the two peaks of $2p_{3/2}$ corresponding to the $Fe^{3+}(O_h)$ and $Fe^{3+}(T_d)$ valence states, respectively (Fig. 2a). Moreover, the presence of two binding energy peaks is a result of Fe^{3+} forming octahedral (O_h) and tetrahedral (T_d) bonds with oxygen.[44] The core-level Co 2p spectra contain two major peaks related to Co $2p_{3/2}$ and Co $2p_{1/2}$, which are further deconvoluted into four peaks (Fig. 2b). The first pair of peaks with lower binding energy signifies the presence of Co^{3+}. In contrast, the second pair of peaks with higher binding energy indicate the Co^{2+} valence state.[45] The Zn 2p core-level spectrum was fitted into two prominent peaks corresponding to Zn $2p_{3/2}$ and Zn $2p_{1/2}$, with the obtained binding energies indicating the Zn^{2+} valence state (Fig. 2c).[46] Further, O 1s spectrum was deconvoluted into three peaks around 529.5 eV, 530.8 eV, and 531.8 eV, corresponding to metal-bonded oxygen (M–O), aluminium-bonded oxygen (Al–O), and adsorbed oxygen (O_{ads}), respectively (Fig. S1b†).[47] In addition, the Al 2p spectrum exhibits two prominent peaks around

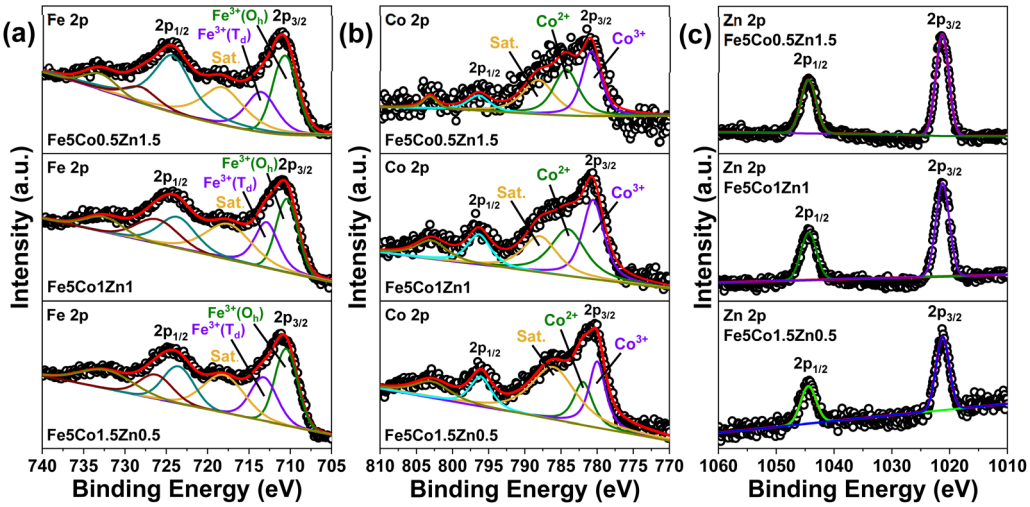

Fig. 2 Core-level XPS spectra: (a) Fe2p, (b) Co 2p, (c) Zn 2p of trimetallic Fe5–Co–Zn/γ-Al_2O_3 nanocatalysts.

73 eV and 75 eV that resemble the Al^{3+} valence state and Al–OH, respectively (Fig. S1c†).[47,48] So, the obtained results indicated that the valence states present in freshly synthesized trimetallic nanocatalysts are Fe^{3+}, Co^{3+}, Co^{2+}, Zn^{2+}, and Al^{3+}, which further suggests that O is chemically bonded to Fe, Co, Zn, and Al in the form of Fe–O, Zn–O, Co–O, and Al–O.

The Brunauer–Emmett–Teller (BET) surface area (S_{BET}), pore width, and pore volume of the Fe5–Co–Zn/γ-Al_2O_3 NCs with varying Co and Zn wt% ratios were determined using N_2 adsorption–desorption isotherms (Fig. S2†). All the synthesized NCs displayed a type IV isotherm with an H3 hysteresis loop, signifying their predominantly mesoporous structure (inset Fig. S2†). The S_{BET}, pore width, and pore volume of the NCs vary based on the stoichiometric ratio of Co and Zn, as shown in Table 1. As the Zn wt% increased, the S_{BET} values decreased, indicating the formation of larger particles and a resulting reduction in the surface-to-volume ratio. The pore width of the NCs was determined using the Barrett–Joyner–Halenda (BJH) method, revealing that the pore width of the trimetallic Fe5Co1.5Zn0.5, Fe5Co1Zn1, and Fe5Co0.5Zn1.5 NCs is increased with a decrease in Co wt% and an increase in Zn wt%, which might be due to the inter-particle pores formation. Moreover, the pore width of bimetallic Fe5Co2Zn0 and Fe5Co0Zn2 NCs suggested that the Zn-containing NCs formed a bigger pore. Furthermore, the pore width of the synthesized trimetallic NCs is substantially greater than the molecular size of CH_4 (0.436 nm), leading to better surface adsorption, which further increases the CH_4 decomposition rate into H_2 and CNTs.

Table 1 Specific surface area (S_{BET}), pore volume, and pore width of Fe5–Co–Zn/γ-Al_2O_3 NCs synthesized using different ratios of Co and Zn

Nanocatalysts	S_{BET} ($m^2\ g^{-1}$)	Pore volume ($cm^3\ g^{-1}$)	Pore width (nm)
Fe5Co2Zn0	40.3	0.230	24.1
Fe5Co1.5Zn0.5	36.1	0.211	19.0
Fe5Co1Zn1	31.8	0.193	25.1
Fe5Co0.5Zn1.5	27.7	0.192	29.8
Fe5Co0Zn2	26.2	0.175	28.9

The surface morphology of Fe5–Co–Zn/γ-Al_2O_3 NCs was analyzed using field-emission scanning electron microscopy (FE-SEM) micrographs (Fig. S3†). The micrograph of Fe5Co2Zn0 displays a bead-like structure with some flakes stacked on the surface, indicating the formation of a hetero-structured morphology (Fig. S3a†). As the Zn content increases to 15% and Co decreases to 5% (Fe5Co1.5Zn0.5 to Fe5Co0.5Zn1.5), the density of the stacked flakes increases (Fig. S3(b)–(d)†). However, the flakes became more prominent when Zn content was further increased to 20% (Fe5Co0Zn2) (Fig. S3e†). So, the obtained micrographs suggested that the Zn promotes the formation of a more flake-like structure on the bead-like surface. Further, the TEM micrograph of NCs confirms the growth of irregular flake structures with variable sizes (Fig. S4†). The high-resolution TEM (HR-TEM) micrograph displays that the flakes are more uniformly distributed in trimetallic Fe5Co1.5Zn0.5, Fe5Co1Zn1, and Fe5Co0.5Zn1.5 NCs (Fig. S4e, h and k†). However, the bimetallic Fe5Co2Zn0 and Fe5Co0Zn2 NCs show the stacked small flakes growth with variable shapes and sizes (Fig. S4b and n†). The selected area electron diffraction (SAED) patterns of Fe5–Co–Zn/γ-Al_2O_3 NCs showed that the polycrystalline in nature (Fig. S4c, f, i, l and o†).

Further, the Fe, Co, and Zn content in the freshly synthesized Fe5Co2Zn0 to Fe5Co0Zn2 NCs was measured using inductively coupled plasma optical emission spectroscopy (ICP-OES). The procedure entailed digesting 2 mg of the sample in aqua regia for 6 hours, followed by dilution prior to measurement. The ICP-OES analysis revealed that the concentrations of cobalt (Co) and zinc (Zn) varied according to the stoichiometric ratios of Co and Zn employed during catalyst synthesis (Table S4†).

3.2 Temperature programmed reduction analysis

The temperature-programmed reduction (TPR) analysis was performed to investigate the reduction behaviour of the

synthesized NCs (Fig. S5†). An amount of ~0.03 g of NCs was placed in a U-tube holder, and the sample was subjected to degassing at a temperature of 200 °C by purging the sample with argon gas to eliminate any remaining gases for 2 hours. Afterward, a blend of 5% H_2 and 95% Ar gases, with a 75 mL min^{-1} flow rate, was circulated through the samples. Then, the sample temperature was thoroughly raised from 60 to 900 °C at a heating rate of 10 °C per minute to acquire the TPR profiles. The Fe5Co2Zn0 to Fe5Co0Zn2 transition peak appeared below 400 °C, indicating the reduction of Co_3O_4 to CoO, and a sharp peak at 460 °C for reducing CoO to metallic cobalt (Co). The broad peak exhibited at around 750 °C and shifted to a higher temperature with an increase in the Zn wt% along with a decrease in the Co wt% identified as the reduction of agglomerated a ZnO and Fe_2O_3 to metal with minimal interaction with γ-Al_2O_3. Furthermore, Zn predominantly forms oxides with lower reducibility (*e.g.*, ZnO) compared to Co oxides (*e.g.*, Co_3O_4 or CoO), which contributes to the increased difficulty of reduction as the Zn wt% is elevated, thereby shifting the reduction temperature to higher values. Furthermore, the TPR profiles exhibited two distinct reduction peaks, occurring between 400–500 °C and around 650 °C (Fig. S5†). For samples with up to 15% Zn (Fe5Co0.5Zn1.5), the reduction peak in the 400–500 °C range shifted to lower temperatures, indicating improved reducibility of the mixed oxide phase due to higher Zn content. However, when Zn content increased to 20%, the reduction peak shifted back to higher temperatures. This demonstrates that an optimal Zn concentration is essential for maximizing catalytic activity, as excessive Zn may either dilute active sites or form stable, non-reducible phases, thereby lowering performance. Additionally, Zn influences the electron density around Fe and Co atoms in Fe5–Co–Zn/γ-Al_2O_3 nanocatalysts. This modification weakens the strong adsorption of carbonaceous intermediates like CH_x species in CMD, which contribute to coke formation. Consequently, carbon precursors desorb more readily, minimizing coke deposition. So, the TPR results show the Zn content plays a significant role in maximizing the catalytic efficiency of Fe5–Co–Zn/γ-Al_2O_3 NCs.

3.3 Methane decomposition and turquoise hydrogen production

The catalytic performance of synthesized NCs (Fe5Co2Zn0 to Fe5Co0Zn2) was investigated by assessing their capability to promote the decomposition of CH_4 to turquoise H_2 and CNTs (Fig. 3). The synthesized trimetallic Fe5Co1.5Zn0.5 to Fe5Co0.5Zn1.5 NCs shown an increasing trend in CH_4 conversion with an increase in Zn content from 5 to 15 wt% and decrease in Co content from 15 to 5 wt% (Fig. 3a and Table S5†). Further, the increase in Zn content to 20 wt% (Fe5Co0Zn2) led to a decrease in CH_4 conversion. However, the CH_4 conversion achieved by the bimetallic Fe5Co2Zn0 NCs is higher than that of Fe5Co0Zn2, potentially due to the distinct reduction behavior of Co_3O_4 and ZnO during the reaction, as discussed in the TPR analysis (Fig. S5†). The maximum conversion of CH_4 using trimetallic Fe5Co1Zn1 and Fe5Co0.5Zn1.5 NCs reached 90% within 25 minutes (Fig. 3a). However, the conversion of CH_4 using Fe5Co2Zn0, Fe5Co1.5Zn0.5, and Fe5Co0Zn2 NCs was determined to be 78.5%, 75.6%, and 72.7%, respectively, in 25 minutes. Furthermore, it was observed that the conversion of CH_4 gradually decreased as the reaction time increased to 150 minutes might be due to the formation of CNTs on the catalyst surface, which may have reduced the availability of active sites (Fig. 3b). Among all the NCs, Fe5Co0.5Zn1.5 exhibited the highest CH_4 conversion and stability up to 150 minutes of reaction time. The maximum CH_4 conversion for Fe5Co0.5Zn1.5 decreased from 90% to 75.94% as the reaction time was increased to 150 minutes, which is significantly higher than other synthesized NCs (Fig. 3b). So, the obtained result underscores the superior efficiency of Fe5Co0.5Zn1.5 in methane decomposition for H_2 production as a fuel and CNTs as a by-product.

Similarly, the trimetallic Fe5Co1.5Zn0.5 to Fe5Co0.5Zn1.5 NCs exhibit an increasing trend in H_2 yield with an increase in Zn content from 5 to 15 wt% and a decrease in Co content from 15 to 5 wt% (Fig. 3c). However, further increasing the Zn content to 20 wt% (Fe5Co0Zn2) results in a decrease in H_2 yield. The highest H_2 yield, 92.2%, was achieved for trimetallic Fe5Co0.5Zn1.5 after 25 minutes of reaction time. The H_2 yields for Fe5Co2Zn0, Fe5Co1.5Zn0.5, Fe5Co1Zn1, and Fe5Co2Zn0 NCs were 79.4%, 77.2%, 91.7%, and 73.3%, respectively.

The H_2 yield slightly decreased after the reaction time reached 150 minutes, which closely aligns with the trends observed in CH_4 conversion. The reduction after 25 minutes of reaction time in CH_4 conversion and H_2 yield can be attributed to the formation of encapsulating carbon, which obstructs access to active sites by covering their surfaces (Fig. 3d). Specifically, the maximum H_2 yield for Fe5Co0.5Zn1.5 NCs decreased from 92.2% to 67.2% (Table S6†).

The selectivity of H_2 production is determined by comparing the actual amount of hydrogen generated to the theoretical amount expected from the catalytic decomposition of CH_4. The calculation of H_2 selectivity is based on eqn (4);

$$H_2 \text{ selectivity } (\%) = \frac{\text{actual } H_2 \text{ produced}}{\text{theoretical } H_2 \text{ produced}} \times 100 \quad (4)$$

H_2 selectivity was determined at the point of maximum CH_4 conversion (25 minutes). It is observed that the H_2 selectivity of trimetallic NCs is increased as the Co wt% decreased from 15 to 5% (Table 2). The trimetallic Fe5Co0.5Zn1.5 exhibited the highest selectivity, achieving 92.1% for H_2 production. Furthermore, the findings indicate that the CH_4 conversion efficiency and H_2 production performance of the synthesized nanocatalysts at elevated temperatures (750 °C) are significantly affected by the tuning of the active metal's ratio (Co and Zn). The CH_4 decomposition reaction was also repeated up to two times using the synthesized NCs, and the CH_4 conversion (%) and H_2 yield (%) remained consistent across the second and third trials, demonstrating the reproducibility of the experiments (Table S7†). Additionally, the obtained CH_4 conversion and H_2 yields are significantly higher than the various previously reported catalysts, including Co/SiO_2, Co/Nb_2O_5, 60% Fe/Al_2O_3, 60% Fe/CeO_2, Co/γ-Al_2O_3, Zn–Co–Fe_2O_3, and

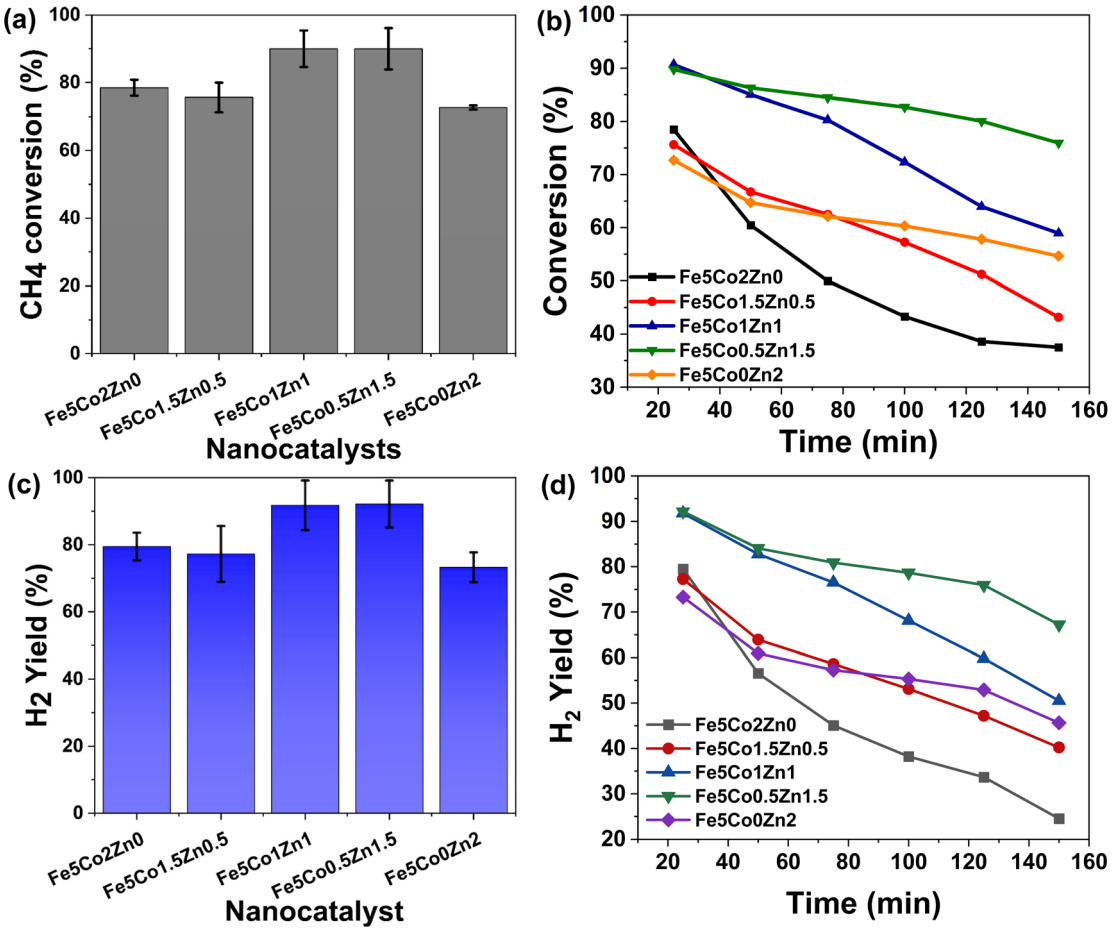

Fig. 3 Methane conversion and yield using different synthesized nanocatalysts: (a) CH_4 conversion at 25 minutes, (b) CH_4 conversion at different time intervals, (c) H_2 yield at 25 minutes, and (d) H_2 yield at different time intervals.

$ZnFe_2O_4$.[18,27,28,30–32] Moreover, a comparison table of conversion, yield, and reaction time of some other previously reported results is presented in Table S8.† The turnover frequency (TOF) at 150 min was also determined to elaborate on the effectiveness of the nanocatalyst for H_2 production. The TOF was determined by calculating the active sites of the catalysts using H_2 temperature-programmed desorption analysis, and the corresponding values are presented in Table S9.†[49] The Fe5Co0.5Zn1.5 gave the maximum active sites of 0.068 mmole/gram; however, Fe5Co1Zn1 gave the maximum TOF as 165.4 h^{-1} at 150 minutes with active sites of 0.051 mmole $gram^{-1}$. The TOF of the most efficient catalyst, Fe5Co0.5Zn1.5, was determined as 156.5 h^{-1} at 150 minutes, suggesting that not all active sites are involved in the reaction might be due to the lower flow rate of CH_4 during reaction. However, Fe5Co0.5Zn1.5 provided maximum CH_4 conversion and H_2 yields (Fig. 3). Further, it was noted that the active sites value of the catalyst is raised to Fe5Co0.5Zn1.5 and decreased by further increase of Zn content to Fe5Co0Zn2. So, the obtained results indicate that suitable Co and Zn are beneficial to achieve better active sites and stability for CH_4 conversion.

As we discussed earlier, along with H_2, the solid carbon was also formed as a by-product in a catalytic CH_4 decomposition reaction. So, the carbon content in spent catalysts was determined using CHNS analysis after 150 minutes of reaction time. The obtained results indicate that the carbon content increased in S-Fe5Co2Zn0 to S-Fe5Co0.5Zn1.5 and then decreased in Fe5Co0Zn2 with a maximum carbon content of 56.38% in S-

Table 2 Hydrogen selectivity at maximum CH_4 conversion using Fe5Co2Zn0 to Fe5Co0Zn2

S. No.	Nanocatalyst	Actual H_2 produced (millimoles)	Theoretical H_2 produced (millimoles)	Selectivity of H_2 (%)
1	Fe5Co2Zn0	0.473	0.595	79.5
2	Fe5Co1.5Zn0.5	0.460	0.595	77.3
3	Fe5Co1Zn1	0.546	0.595	91.7
4	Fe5Co0.5Zn1.5	0.548	0.595	92.1
5	Fe5Co0Zn2	0.436	0.595	73.2

Table 3 Elemental analysis of spent nanocatalysts of S-Fe5Co2Zn0 to S-Fe5Co0Zn2

S. No.	Sample weight (mg)	Nanocatalysts	N [%]	C [%]	H [%]	S [%]
1	2.38	S-Fe5Co2Zn0	0.01	33.40	0.05	0.01
2	2.73	S-Fe5Co1.5Zn0.5	0	44.74	0.05	0.03
3	2.10	S-Fe5Co1Zn1	0.01	50.04	0.05	0.04
4	2.24	S-Fe5Co0.5Zn1.5	0	56.38	0.06	0.04
5	2.62	S-Fe5Co0Zn2	0.01	49.26	0.05	0.05

Fe5Co0.5Zn1.5 (Table 3). The amounts of hydrogen (H), nitrogen (N), and sulfur (S) were minimal compared to carbon. The analysis also suggested that trimetallic Fe5Co0.5Zn1.5 promotes the maximum CNTs formation and highest yield of H_2. Additionally, the amount of CNTs produced is influenced by the quantity of H_2 generated and the duration of the reaction. So, the obtained results suggest that the Co and Zn ratios play a crucial role in determining the selectivity, quantity, and quality of the products.

Powder X-ray diffraction analysis of reduced and spent Fe5Co2Zn0 to Fe5Co0Zn2 was performed to identify the changes in phase and crystallographic structure after 150 minutes of reaction time (Fig. 4). The obtained diffraction pattern of the reduced as well as spent NCs reveals the most intense peaks around $2\theta = 44°$, which is corresponds to the planes (111) of the cubic phase of metallic γ-Fe with the space group of $Fm\bar{3}m$ (JCPDF no. 005-3803, $a = b = c = 3.61$ Å) and cubic phase of metallic α-Co with the space group of $Fm\bar{3}m$ (JCPDF no. 004-4989, $a = b = c = 3.54$ Å). When the Zn content increased up to 20 wt%, a new diffraction peak appeared at $2\theta = 36.7°$, which is aligned with the (002) plane of the hexagonal phase of metallic Zn with space group of $P6_3/mmc$ (JCPDF no. 042-1013, $a = b = c = 2.66$ Å). In Fig. 4b, the spent NCs showed another diffraction peak at $2\theta = 26°$ of the (002) plane, which is well matched with the hexagonal phase of carbon (C1) with the space group $P63/mmc$ (JCPDS no. 061-7290, $a = b = 2.47$ Å, $c = 6.93$ Å). So, the obtained diffraction patterns suggested that the freshly synthesized bimetallic and trimetallic metal oxide NCs are reduced to their metallic phase during and after the catalytic CH_4 decomposition reaction.

Raman spectroscopy was employed to investigate the degree of graphitization and crystallinity of the deposited CNTs. In the Raman spectra, two clear bands can be observed, one near ~1570 cm^{-1} (referred to as the G-band), which is linked to the graphitization process and results from in-plane lattice vibrations of the C=C (sp^2) bond (Fig. 5a). The additional band, noted at ~1340 cm^{-1} (D-band), resulted from the structural disorder present in the graphene structure. The intensity ratio of the D and G-band can reveal the quality of CNTs, as it is linked to the degree of structural disorder in the material. The spectral data, which included D- and G-band intensities, were converted into ratios (I_D/I_G). The minimum value of I_D/I_G is 0.37 for S-Fe5Co0.5Zn1.5, whereas the highest value is 0.49 for both S-Fe5Co2Zn0 and S-Fe5Co1.5Zn0.5. The I_D/I_G values varied from 0.37 to 0.49 for S-Fe5Co2Zn0 to S-Fe5Co0Zn2, as presented in Table S10.† The Raman findings indicated that the formation of CNTs was successfully achieved, and the quality of CNTs can be modified by adjusting the stoichiometric ratio of Co and Zn in the nanocatalyst.

To further investigate the functional characteristics of CNTs, FTIR spectroscopy was performed in the range of 550–4000 cm^{-1} of S-Fe5Co2Zn0 to S-Fe5Co0Zn2 (Fig. 5b). A broad band observed at 3442 cm^{-1} was attributed to hydrogen-bonded O–H groups from moisture. The two separate peaks at 2980–2820 cm^{-1} were associated with the asymmetric and symmetric stretching of the C–H bond. The peaks between 1490–1350 cm^{-1} can be ascribed to asymmetric bending vibration of the C–H bond. The band appeared around 1740 cm^{-1} corresponding to the stretching vibration of the C=O bond. Additionally, the band at ~1627 cm^{-1} is stretching vibration of aromatic C=C bonds in the sp^2 carbon domain.[41] The three

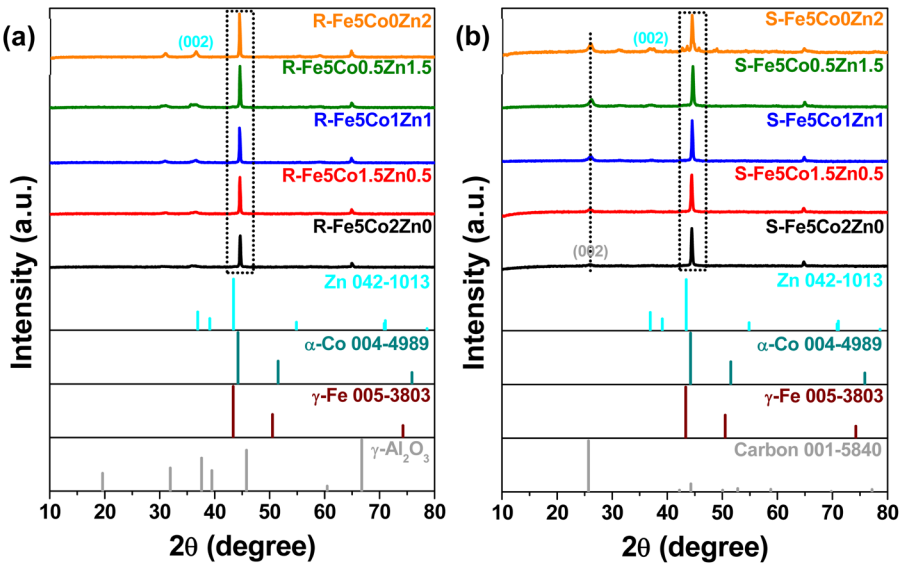

Fig. 4 Powder-XRD diffraction patterns: (a) reduced Fe5–Co–Zn/γ-Al_2O_3, and (b) spent Fe5–Co–Zn/γ-Al_2O_3 NCs.

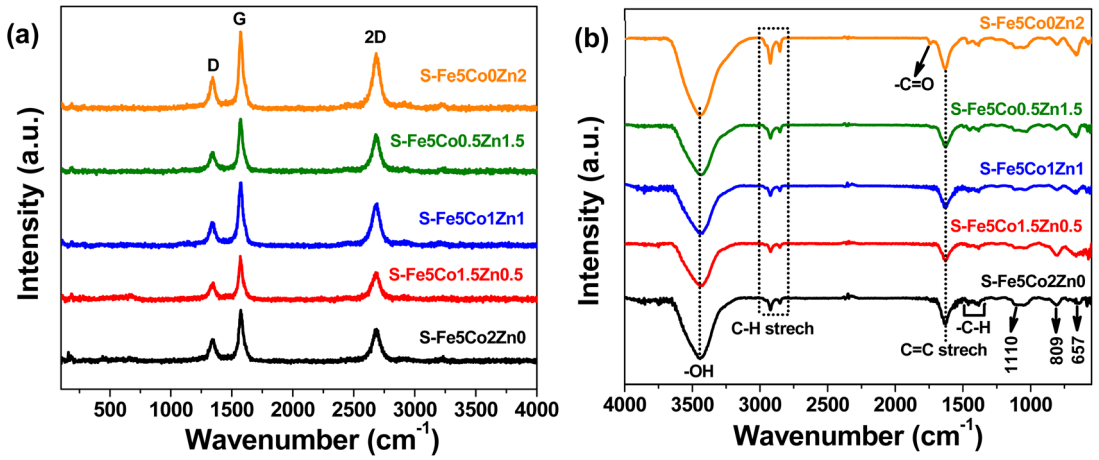

Fig. 5 (a) Raman spectra of the in the spectral range 100 cm^{-1}–4000 cm^{-1} ($\lambda = 532$ nm), and (b) FTIR patterns of the spent nanocatalyst of S-Fe5Co2Zn0 to S-Fe5Co0Zn2.

peaks observed at 1110, 809, and 657 cm^{-1} were assigned to the stretching vibration of the –O–R group, the aromatic out-of-plane C–H deformations, and the M–O bond, respectively.[50]

The morphology of spent Fe5–Co–Zn/γ-Al_2O_3 NCs was examined using FE-SEM micrographs (Fig. 6 and S6†). The micrographs of bimetallic S-Fe5Co2Zn0 show that the nanotubes are spread on the surface of catalysts (Fig. S6a†). In the trimetallic NCs, as the Zn content increases to 15% and Co decreases to 5% (Fe5Co1.5Zn0.5 to Fe5Co0.5Zn1.5), the density of the nanotubes significantly increases (Fig. 6d). Further increase in Zn content to 20% (Fe5Co0Zn2), the nanotubes density on the surface of the catalyst is slightly decreased (Fig. S6b†). It is displayed that the trimetallic S-Fe5Co0.5Zn1.5 formed more prominent nanotubes. To further analyse the morphology of CNTs, TEM micrographs of the S-Fe5Co2Zn0 to S-Fe5Co0Zn2 are assessed to elaborate the morphological characteristic at higher resolution. The obtained results revealed that the length and quality of CNTs are significantly influenced by the stoichiometric ratio of Co and Zn (Fig. 6d–f, S7 and S8†). The micrographs showed that as the Zn content increased to 15% and Co decreased to 5%, the nanotube length and uniformity improved. However, when the Zn content reached 20%, the growth of CNTs became distorted. Notably, the S-Fe5Co0.5Zn1.5 produced more uniform CNTs compared to the other synthesized NCs (Fig. 6d and S8†). The inset micrographs of Fig. 6 and S7† display that the CNTs are wrapped around the tops of the catalyst particles, indicating multi-walled carbon nanotubes (MWCNTs) formation, which seems to be grown by a base-growth mechanism.[51] The HR-TEM micrographs of S-Fe5Co2Zn0 to S-Fe5Co0Zn2 revealed

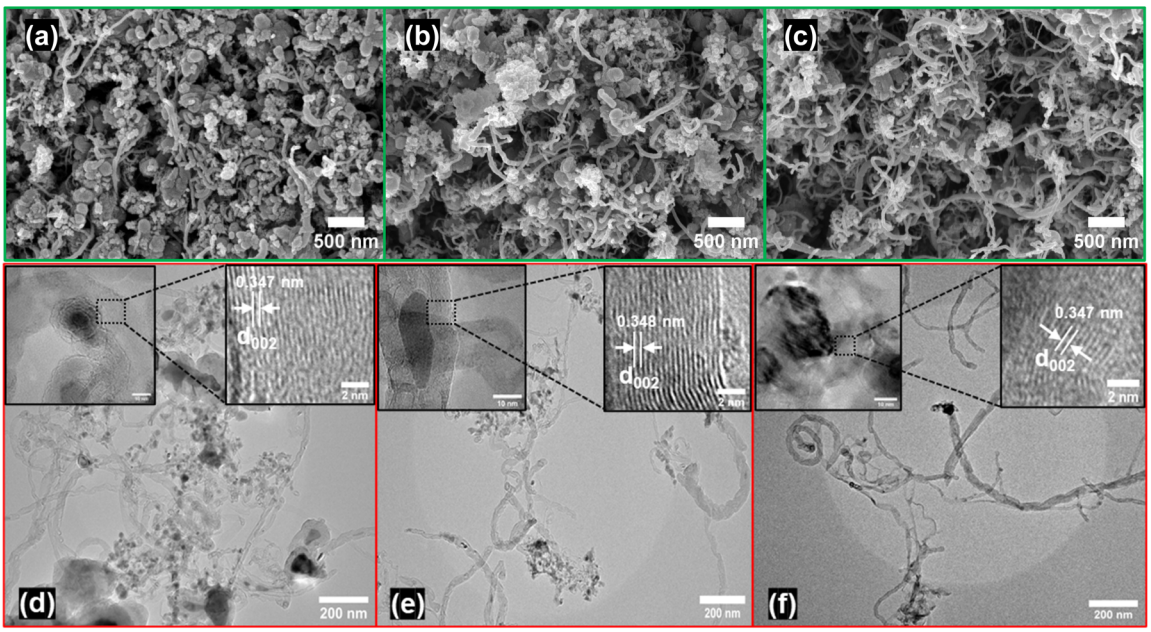

Fig. 6 FE-SEM micrographs of spent-trimetallic nanocatalysts (a) S-Fe5Co1.5Zn0.5, (b) S-Fe5Co1Zn1, (c) S-Fe5Co0.5Zn1.5.

characteristic fringes of CNTs, with the interplanar spacing in the region denoted by a black dotted box measured at 0.346 to 0.348 nm. These values correspond to the (002) plane of hexagonal carbon (C1) and are consistent with our powder-XRD results (inset Fig. 6d–f and inset Fig. S7†). The SAED patterns of S-Fe5Co2Zn0 to S-Fe5Co0Zn2 confirm the polycrystalline nature of the NCs (Fig. S9†). The STEM-EDS elemental mappings show a uniform distribution of carbon (C) and metals across the catalyst surface, indicating the stability and formation of high-quality CNTs (Fig. S10a–e†). The oxygen observed in the spent NCs is attributed to the presence of γ-Al_2O_3 and the adsorption of atmospheric moisture on the surface.

The XPS analysis of our best catalyst (S-Fe5Co0.50Zn1.5) was performed to investigate the chemical composition and electronic state on the surface after the CH_4 decomposition reaction for 150 minutes (Fig. 7). The survey spectrum peaks clearly revealed that the S-Fe5Co0.5Zn1.5 consists of iron (Fe), cobalt (Co), zinc (Zn), carbon (C), aluminium (Al), and oxygen (O), elements (Fig. S11†). To examine the valence states within the S-Fe5Co0.5Zn1.5, the core-level spectra of Fe 2p, Co 2p, Zn 2p, C 1s, O 1s, and Al 2p were deconvoluted. The core-level spectrum of Fe 2p is fitted with three peaks of $2p_{3/2}$ at 707.2 eV, 711.3 eV, and 714.1 eV corresponding to the Fe(0), $Fe^{3+}(O_h)$ and $Fe^{3+}(T_d)$ valence states, respectively (Fig. 7a).

The core-level Co 2p spectra contain major peaks related to Co $2p_{3/2}$ with a binding energy of 783.4 eV, which signifies the presence of Co^{2+} valence state (Fig. 7b).[45] The Zn 2p core-level spectrum was fitted into a peak $2p_{3/2}$ at 1022.9 eV indicating the Zn^{2+} valence state (Fig. 7c).[46] The presence of Fe^{3+}, Co^{2+}, and Zn^{2+} in the S-Fe5Co0.5Zn1.5 due to the aerials oxidation of catalysts after reaction. The core-level C 1s spectrum was fitted into three peaks, 284.3 eV, 285.1 eV, and 289.6 eV, indicating the presence of sp^2/sp^3 carbon (C=C/C–C), –C–O, and –COO group of CNTs, which coincides with the origin of D-band in our Raman spectra (Fig. 7d and 5a).[52] Additionally, the O 1s spectrum was deconvoluted into two peaks at approximately 532.2 eV and 533.8 eV, corresponding to adsorbed oxygen (O_{ads}) and water (O_{H_2O}), respectively (Fig. 7e). Furthermore, the Al 2p spectrum shows two distinct peaks near 75.1 eV and 76.2 eV, indicating the presence of Al_2O_3. The obtained XPS binding energies reveal downshifts in the binding energies of Fe 2p and Co 2p in S-Fe5Co0.5Zn1.5 compared to fresh Fe5Co0.5Zn1.5 (Table S2†), indicating elevated electron density at the Fe and Co centres. This is attributed to electron donation from Zn^{2+} ions ($3d^{10}$ electronic configuration), which facilitate charge redistribution within the multi-metallic system. In the Fe5Co0.5Zn1.5 nanocatalyst, a decrease in Co^{2+} concentration was observed, while in the spent catalyst, an increase in Co^{3+} concentration was observed, as shown in Table S11.† This indicates electron transfer between Co and Fe during the reaction. Similarly, for Fe species, the concentration of $Fe^{3+}(O_h)$ sites decreased, whereas the $Fe^{3+}(T_d)$ sites increased, suggesting a redistribution of electrons and coordination environment, further supporting the occurrence of metal–metal electronic interactions within the catalyst. So, the synergistic effect between Fe, Co, and Zn plays significant role in the CH_4 decomposition to turquoise H_2 and CNTs productions.

3.4 Separation of carbon nanotubes

The separation of pure CNTs from spent catalysts following the methane decomposition reaction presents a significant challenge and is essential for their effective industrial application. To separate the carbon nanotubes, we have chosen our best spent nanocatalyst S-Fe5Co0.5Zn1.5. The obtained spent nanocatalyst powder is mixed with 1 mmole aqueous solution of sodium

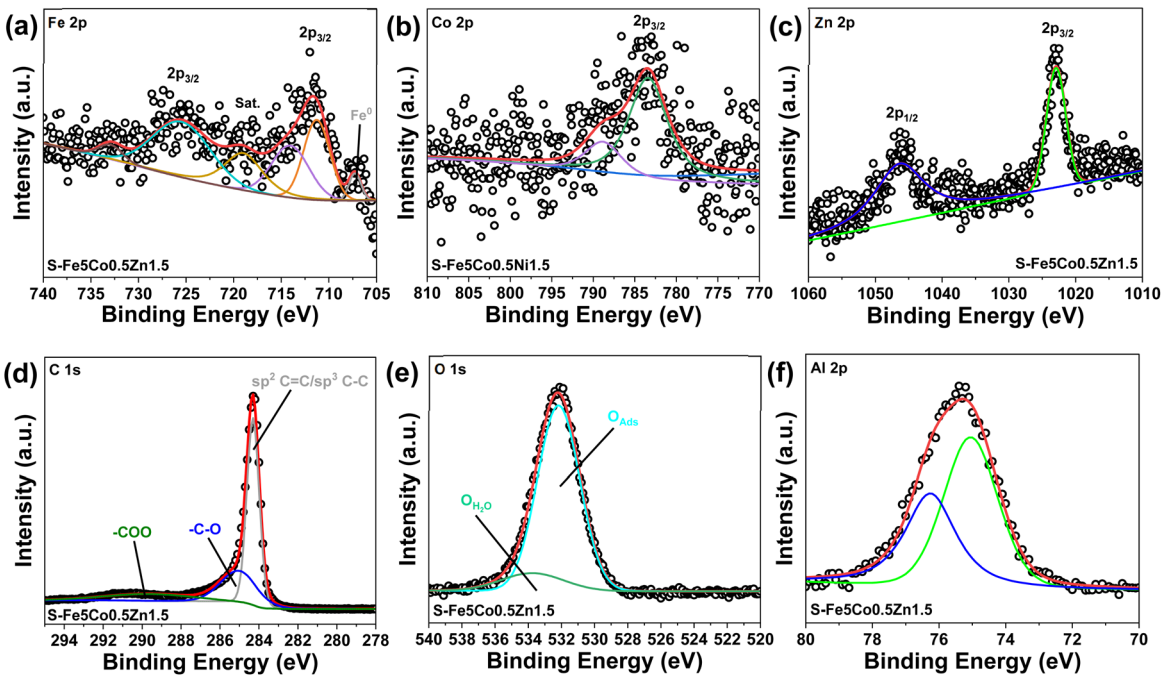

Fig. 7 XPS core-level spectra: (a) Fe 2p, (b) Co 2p, (c) Zn 2p, (d) C 1s, (e) O 1s, and (f) 2p of S-Fe5Co0.5Ni1.5.

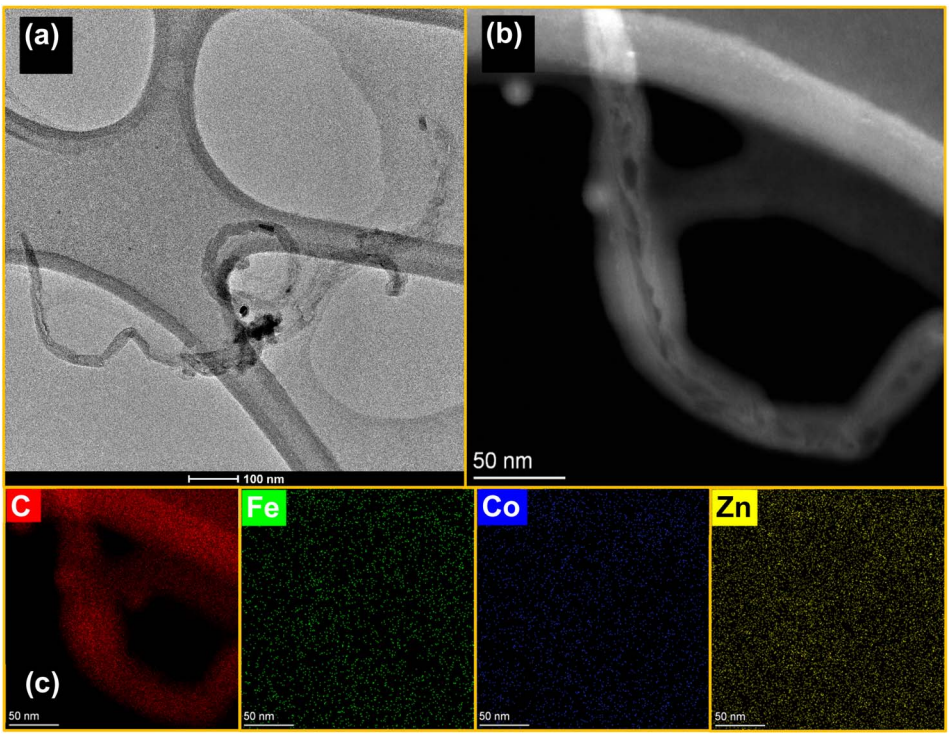

Fig. 8 (a) TEM micrograph of CNTs, (b) dark-field micrograph of CNTs, and (c) STEM-EDS image mapping of separated CNTs from S-Fe5Co0.5Zn1.5.

dodecyl sulfate ($CH_3(CH_2)_{11}SO_4Na$) in 15 mL and sonicated for 1 hour. Further, CNTs are separated from the catalyst using a neodymium (Nd) magnet and dried in vacuum oven for 6 hours to obtained final product. To further examine the quality of CNTs, TEM micrographs of the separated carbon nanotubes is obtained. The micrograph displays the CNTs spread on the surface of the carbon grid with minute amount of nanocatalyst particles (Fig. 8a). Furthermore, the high-angle annular dark-field (HAADF) micrograph of CNTs indicates that the formation of multi-walled nanotubes (Fig. 8b). Additionally, the STEM-EDS image mapping revealed the uniform distribution of carbon (C) on separated CNTs without presence of Fe, Co, and Zn (Fig. 8c). Thus, the results confirm that the separated CNTs are free from nanocatalyst contamination and high in quality.

4 Conclusion

In summary, trimetallic Fe5–Co–Zn/γ-Al_2O_3 NCs were synthesized by controlling the stoichiometric ratio of the Co and Zn wt% from 0 to 20% using a co-precipitation approach followed by calcination at 750 °C under atmospheric conditions. The synthesis process avoided the use of hazardous chemicals and did not require a specialized reaction setup like an inert atmosphere. The powder diffraction patterns, and Raman Spectra revealed that the freshly synthesized trimetallic NCs composed of hexagonal Fe_2O_3, cubic Co_3O_4, and hexagonal ZnO without producing a significant solid solution between Fe, Co, and Zn. The Fe5–Co–Zn/γ-Al_2O_3 NCs showed excellent CH_4 decomposition ability with Co/Zn stoichiometric ratio-dependent H_2 and CNTs production. The NCs having 5% Co and 15% Zn (Fe5Co0.5Zn1.5), exhibited the highest CH_4 conversion, H_2 yield, H_2 selectivity, and CNTs production of 90%, 92.2%, 92.15%, and carbon (C) of 56.4%, respectively, which are better than many other previously reported results. The Raman and electron microscopic studies revealed the length, uniformity, and quality of CNTs are significantly dependent on the stoichiometric ratio of Co and Zn in NCs. Among all synthesized NCs, trimetallic Fe5Co0.5Zn1.5 NCs produced the most uniform and high-quality CNTs. The produced CNTs are wrapped around the tops of the catalyst particles and form multi-walled carbon nanotubes (MWCNTs), which are plausibly grown by a base-growth mechanism. This study introduces a straightforward synthesis approach for structurally controlled trimetallic catalysts and provides insights into the behavior of active metal ratios on the catalysts surface, facilitating the design of optimized catalysts for efficient turquoise H_2 and CNT production.

Data availability

The data supporting the findings of this study can be found in the ESI† of this paper.

Conflicts of interest

It is declared by the authors that they do not have any known competing financial interests or personal ties that could have appeared to affect the work that is disclosed in this paper.

Acknowledgements

EA would like to thank the Vashisht Foundation for a CoE grant to set up the Naresh Vashisht Centre for Hydrogen and CCUS Technologies at IIT(ISM) Dhanbad.

References

1 I.-W. Wang, D. A. Kutteri, B. Gao, H. Tian and J. Hu, *Energy Fuels*, 2019, **33**, 197–205.
2 A. M. Abdalla, S. Hossain, O. B. Nisfindy, A. T. Azad, M. Dawood and A. K. Azad, *Energy Convers. Manage.*, 2018, **165**, 602–627.
3 M. Pudukudy, Z. Yaakob, M. Mohammad, B. Narayanan and K. Sopian, *Renewable Sustainable Energy Rev.*, 2014, **30**, 743–757.
4 A. Antzara, E. Heracleous, D. B. Bukur and A. A. Lemonidou, *Int. J. Greenhouse Gas Control*, 2015, **32**, 115–128.
5 R. Kumar, R. Singh and S. Dutta, *Energy Fuels*, 2024, **38**, 2601–2629.
6 P. Ammendola, R. Chirone, L. Lisi, G. Ruoppolo and G. Russo, *J. Mol. Catal. A: Chem.*, 2007, **266**, 31–39.
7 L. Fan, Z. Tu and S. H. Chan, *Energy Rep.*, 2021, **7**, 8421–8446.
8 N. S. Hassan, A. A. Jalil, S. Rajendran, N. F. Khusnun, M. B. Bahari, A. Johari, M. J. Kamaruddin and M. Ismail, *Int. J. Hydrogen Energy*, 2024, **52**, 420–441.
9 N. J. Rubinsin, N. A. Karim, S. N. Timmiati, K. L. Lim, W. N. R. W. Isahak and M. Pudukudy, *Int. J. Hydrogen Energy*, 2024, **49**, 1139–1164.
10 F. Dai, S. Zhang, Y. Luo, K. Wang, Y. Liu and X. Ji, *Processes*, 2023, **11**, 1765.
11 S. R. Patlolla, K. Katsu, A. Sharafian, K. Wei, O. E. Herrera and W. Mérida, *Renewable Sustainable Energy Rev.*, 2023, **181**, 113323.
12 A. Boretti and B. K. Banik, *Adv. Energy Sustainability Res.*, 2021, **2**, 1–10.
13 A. Holmen, *Catal. Today*, 2009, **142**, 2–8.
14 Z. Taherian, A. Khataee, N. Han and Y. Orooji, *J. Ind. Eng. Chem.*, 2022, **107**, 20–30.
15 D. H. Lee, H. Kang, Y. Kim, H. Song, H. Lee, J. Choi, K.-T. Kim and Y.-H. Song, *Fuel Process. Technol.*, 2023, **247**, 107761.
16 Z. Fan, W. Weng, J. Zhou, D. Gu and W. Xiao, *J. Energy Chem.*, 2021, **58**, 415–430.
17 T. Geißler, A. Abánades, A. Heinzel, K. Mehravaran, G. Müller, R. K. Rathnam, C. Rubbia, D. Salmieri, L. Stoppel, S. Stückrad, A. Weisenburger, H. Wenninger and T. Wetzel, *Chem. Eng. J.*, 2016, **299**, 192–200.
18 R. R. C. M. Silva, H. A. Oliveira, A. C. P. F. Guarino, B. B. Toledo, M. B. T. Moura, B. T. M. Oliveira and F. B. Passos, *Int. J. Hydrogen Energy*, 2016, **41**, 6763–6772.
19 V. Nichele, M. Signoretto, F. Menegazzo, A. Gallo, V. Dal Santo, G. Cruciani and G. Cerrato, *Appl. Catal., B*, 2012, **111–112**, 225–232.
20 N. S. N. Hasnan, S. N. Timmiati, K. L. Lim, Z. Yaakob, N. H. N. Kamaruddin and L. P. Teh, *Mater. Renew. Sustain. Energy*, 2020, **9**, 8.
21 L. Alves, V. Pereira, T. Lagarteira and A. Mendes, *Renewable Sustainable Energy Rev.*, 2021, **137**, 110465.
22 C. Q. Pham, T. J. Siang, P. S. Kumar, Z. Ahmad, L. Xiao, M. B. Bahari, A. N. T. Cao, N. Rajamohan, A. S. Qazaq, A. Kumar, P. L. Show and D.-V. N. Vo, *Environ. Chem. Lett.*, 2022, **20**, 2339–2359.
23 E. Meloni, M. Martino and V. Palma, *Catalysts*, 2020, **10**, 352.
24 J. X. Qian, T. W. Chen, L. R. Enakonda, D. Bin Liu, G. Mignani, J.-M. Basset and L. Zhou, *Int. J. Hydrogen Energy*, 2020, **45**, 7981–8001.
25 Y. Wang, Y. Zhang, S. Zhao, J. Zhu, L. Jin and H. Hu, *Carbon Resour. Convers.*, 2020, **3**, 190–197.
26 A. Gamal, K. Eid, M. H. El-Naas, D. Kumar and A. Kumar, *Nanomaterials*, 2021, **11**, 1226.
27 P. Yan, K. Zhang and Y. Peng, *Chem. Eng. Sci.*, 2022, **250**, 117410.
28 L. Tang, D. Yamaguchi, N. Burke, D. Trimm and K. Chiang, *Catal. Commun.*, 2010, **11**, 1215–1219.
29 T. E. Bell, H. Ménard, J.-M. González Carballo, R. Tooze and L. Torrente-Murciano, *Int. J. Hydrogen Energy*, 2020, **45**, 27210–27220.
30 A. I. Alharthi, E. Abdel-Fattah, J. S. J. Hargreaves, M. A. Alotaibi, I. U. Din and M. N. Al-Shalwi, *J. Alloys Compd.*, 2023, **938**, 168437.
31 N. D. Evdokimenko, G. I. Kapustin, O. P. Tkachenko, K. B. Kalmykov and A. L. Kustov, *Molecules*, 2022, **27**, 1065.
32 B. A. Al Alwan, M. Shah, M. Danish, M. K. Al Mesfer, M. I. Khan and V. Natarajan, *J. Indian Chem. Soc.*, 2022, **99**, 100393.
33 D. Torres, J. L. Pinilla and I. Suelves, *Int. J. Hydrogen Energy*, 2020, **45**, 19313–19323.
34 L. Zhou, L. R. Enakonda, M. Harb, Y. Saih, A. Aguilar-Tapia, S. Ould-Chikh, J. Hazemann, J. Li, N. Wei, D. Gary, P. Del-Gallo and J.-M. Basset, *Appl. Catal., B*, 2017, **208**, 44–59.
35 M. Hamdan, L. Halawy, N. Abdel Karim Aramouni, M. N. Ahmad and J. Zeaiter, *Fuel*, 2022, **324**, 124455.
36 A. A. Ibrahim, A. H. Fakeeha, A. S. Al-Fatesh, A. E. Abasaeed and W. U. Khan, *Int. J. Hydrogen Energy*, 2015, **40**, 7593–7600.
37 L. Gama, M. A. Ribeiro, B. S. Barros, R. H. A. Kiminami, I. T. Weber and A. C. F. M. Costa, *J. Alloys Compd.*, 2009, **483**, 453–455.
38 F. Pompeo, D. Gazzoli and N. N. Nichio, *Mater. Lett.*, 2009, **63**, 477–479.
39 L. Zardin and O. W. Perez-Lopez, *Int. J. Hydrogen Energy*, 2017, **42**, 7895–7907.
40 K. R. Parmar, K. K. Pant and S. Roy, *Energy Convers. Manage.*, 2021, **232**, 113893.
41 V. G. Hadjiev, M. N. Iliev and I. V Vergilov, *J. Phys. C:Solid State Phys.*, 1988, **21**, L199–L201.
42 J. Thyr, L. Österlund and T. Edvinsson, *J. Raman Spectrosc.*, 2021, **52**, 1395–1405.
43 R. Mo, Q. Liu, H. Li, S. Yang and J. Zhong, *J. Mater. Sci.: Mater. Electron.*, 2019, **30**, 21444–21453.
44 R. S. Yadav, I. Kuřitka, J. Vilcakova, J. Havlica, J. Masilko, L. Kalina, J. Tkacz, V. Enev and M. Hajdúchová, *J. Phys. Chem. Solids*, 2017, **107**, 150–161.

45 A. A. Khan, S. Kumari, A. Chowdhury and S. Hussain, *ACS Appl. Nano Mater.*, 2018, **1**, 3474–3485.
46 A. A. Khan, A. Chowdhury, S. Kumari and S. Hussain, *J. Mater. Chem. A*, 2020, **8**, 1986–2000.
47 K. D. Moulder, J. F. Stickle, W. F. Sobol and P. E. Bomben, *Handbook of X-Ray Photoelectron Spectroscopy*, Perkin - Elmer Corporation, United State of America, 1992.
48 P. M. A. Sherwood, *Surf. Sci. Spectra*, 1998, **5**, 1–3.
49 M. Prasad, K. Ray, A. Sinhamahapatra and S. Sengupta, *J. Mater. Sci.*, 2022, **57**, 2839–2856.
50 C. Liu, K. Shih, Y. Gao, F. Li and L. Wei, *J. Soils Sediments*, 2012, **12**, 724–733.
51 A. M. Amin, E. Croiset and W. Epling, *Int. J. Hydrogen Energy*, 2011, **36**, 2904–2935.
52 T. I. T. Okpalugo, P. Papakonstantinou, H. Murphy, J. McLaughlin and N. M. D. Brown, *Carbon*, 2005, **43**, 153–161.